ORNL/SPR-2023/2889

Elastic Flow Modeling for Hydropower Digital Twins

William Gurecky
Hong Wang
Shawn Ou

Approved for public release.
Distribution is unlimited.

May 2023

OAK RIDGE National Laboratory

ORNL IS MANAGED BY UT-BATTELLE LLC FOR THE US DEPARTMENT OF ENERGY

ORNL/SPR-2023/2889

Buildings and Transportation Science Division

ELASTIC FLOW MODELING FOR HYDROPOWER DIGITAL TWINS

William Gurecky
Hong Wang
Shawn Ou

May 2023

Prepared by
OAK RIDGE NATIONAL LABORATORY
Oak Ridge, TN 37831
managed by
UT-Battelle LLC
for the
US DEPARTMENT OF ENERGY
under contract DE-AC05-00OR22725

CONTENTS

LIST OF FIGURES v
LIST OF TABLES vii
ABBREVIATIONS ix
ABSTRACT 1
1. INTRODUCTION 1
1.1 Conservation of Mass 2
1.2 Newton's Second Law 4
1.3 Equation of State and Wave Speed 5
1.3.1 Wave Speed 6
1.3.2 Vectorized Conservation Law Form 7
1.4 Finite Volume Discretization and Solution Procedure 8
1.4.1 The Riemann Problem 9
1.4.2 Approximate Solution to the Riemann Problem 10
1.4.3 Extrapolating Cell-Centered Values to Faces by MUSCL Reconstruction 10
1.4.4 Time Integration 12
2. TURBINE DYNAMIC MODEL 12
2.1 Torque Balance 13
2.2 Turbine Flow Model 13
2.3 PID control of the Turbine 14
3. RESULTS 15
3.1 Elastic Model Results 17
3.2 Comparison with Inelastic Model Results 22
4. CONCLUSION 26
5. ACKNOWLEDGMENTS 27
6. REFERENCES 28
APPENDIX A. Mesh Convergence Study A-1

LIST OF FIGURES

1 An infinitesimal control volume with length δs, centered at s_o. A_s is the flow area as a function of s. θ is the angle of the pipe, relative to horizontal. 2
2 Finite volume mesh. 9
3 MUSCL scheme with different values of ϕ. 11
4 MUSCL scheme with different flux limiters. 11
5 A Francis turbine with key components shown (Vytvytskyi and Lie [2018]). 13
6 Simplified dam geometry used in flow simulations. Note: not to scale. 16
7 Specified grid load torque profile, T_L, as a function of time. 17
8 Turbine rotation rate set point, ω^*, as a function of time. 17
9 Volumetric flow rate $\dot{V}$ from the elastic flow model as a function of time and space. 18
10 Static gauge pressure from the elastic model as a function of time and space. 18
11 Volumetric flow rate and static gauge pressure distribution at time t = 49.948 s. 19
12 Static gauge pressure at the turbine inlet as a function of time. 19
13 Turbine inlet vane angle vs. time. The set point is from the PID control signal. 20
14 Applied load T_L and shaft torque T_w due to water flow. 20
15 Turbine power as a function of time. 20
16 Turbine rotation rate vs. time. 20
17 Static Δp over the turbine as a function of time. 21
18 Flow rate through turbine vs. time. 21
19 Density, ρ, and local wave speed, a, profiles at t = 50 s. 21
20 Pressure-dependent elastic pipe diameter at t = 50 s. 21
21 Elastic vs. inelastic model turbine flow rate. 22
22 Elastic vs. inelastic model turbine inlet pressure. 22
23 Elastic vs. inelastic model turbine power. 23
24 Elastic vs. inelastic model turbine rotation rate. 23
25 Elastic vs. inelastic model turbine flow rate from t=0 to 8 s. 23
26 Elastic vs. inelastic model turbine inlet pressure from t=0 to 8 s. 23
27 Elastic vs. inelastic model turbine power from t=0 to 8 s. 24
28 Elastic vs. inelastic model turbine rotation rate from t=0 to 8 s. 24
29 Elastic vs. inelastic model turbine flow rate from t=15 to 25 s. 24
30 Elastic vs. inelastic model turbine inlet pressure from t=15 to 25 s. 24
31 Elastic vs. inelastic model turbine power from t=15 to 25 s. 25
32 Elastic vs. inelastic model turbine rotation rate from t=15 to 25 s. 25
33 Smooth wave advection solution at $t = 3(s)$ with mesh spacing $\Delta s = 0.05(m)$. A-2
34 Square wave advection solution at $t = 3(s)$ with mesh spacing $\Delta s = 0.05(m)$. A-2
35 Mesh spacing convergence plot for the smooth wave advection problem A-2
36 Mesh spacing convergence plot for the square wave advection problem. A-2

LIST OF TABLES

1 Model parameters 16
2 Smooth wave mesh convergence results. A-2
3 Square wave mesh convergence results. A-2

ABBREVIATIONS

API	application programming interface
CFD	computational fluid dynamics
KT	Kurganov–Tadmor
MUSCL	Monotonic Upstream-Centered Scheme for Conservation Laws
ODE	ordinary differential equation
PDE	partial differential equation
PID	proportional-integral-derivative

ABSTRACT

This report details the unsteady, 1D conservation equations that are used to model elastic flow through a penstock in a hydropower facility. The elastic flow model is accurate even in cases of fast transients, long penstock length, and high gravitation head. The compressibility of the water and elasticity of the pipe walls are explicitly accounted for in the developed models so that the water hammer phenomena can be accurately captured. The elastic flow model is coupled to a mechanistic turbine model to resolve the dynamic feedback between the elastic water column and the turbine rotation rate.

A finite volume method is employed to solve the governing equations, and the method is shown to have low numerical diffusion in sharp gradient phenomena, such as those encountered when simulating water hammer. The method is applied to single dimensional linear advection benchmark problem and numerical results are compared with analytic results. This is followed on by an application to a full hydropower system with a coupled turbine. The elastic flow model results are compared against an inelastic model.

1. INTRODUCTION

This report builds on prior work focused on inelastic flow modeling of a hydroelectric system, with coupled dynamic penstock and turbine models ([Gurecky et al., 2022]). The inelastic flow model is incapable of accurately capturing fast transient cases where water hammer is present and generally is not accurate for penstocks with a large length. This is because the inelastic flow equations assume a constant water density. In the inelastic model, pressure information propagates instantaneously through the penstock and turbine system, when in reality this is not true, particularly for cases with long penstocks and high gravitational head. If the engineer requires accurate estimates of the pressures and flow velocity at all locations in the system, particularly in fast transient cases, an elastic flow model is required to resolve the water hammer phenomena.

Modeling the elasticity of the water and pipe necessitates solving two coupled partial differential equations (PDEs) governing the mass and momentum conservation of a slightly compressible liquid. The equations are dominated by first-order spatial derivative terms—advection terms—and are hyperbolic in nature. This property guides the selection of the numerical method used to solve the coupled system of equations. This report details a finite volume approach to solving the coupled system of hyperbolic PDEs. A high-order method is employed to solve the equations based on the Monotonic Upstream-Centered Scheme for Conservation Laws (MUSCL) reconstruction and Kurganov–Tadmor (KT) scheme. The resulting numerical method is able to resolve sharp pressure gradients within the system while introducing minimal artificial dissipation.

The model uses a simplified equation of state so that the water density is a linear function of pressure and the pipe diameter is a linear function of pressure. The developed elastic flow model is coupled to a dynamic mechanistic turbine model to compute the rotation rate of the turbine and pressure losses across the turbine. The full nonlinear elastic flow and turbine dynamics are captured and jointly stepped forward in time using a second-order explicit time integration scheme, the midpoint method. The results are contrasted against the simplified inelastic models developed in prior work, and it is shown that the elastic model predicts significantly different peak pressures and flow rates under fast transient conditions; however, in steady-state cases, the two models are in agreement.

The model will be developed from first principles, beginning with the conservation of mass and momentum. First, a control volume analysis is performed on an infinitesimal section of the penstock, with

length δs. In this work, we assume the flow is confined to travel in one dimension, along the penstock centerline with flow area $A_s(s)$ that is a function of distance along the penstock, s. The influence of 3D flow features and turbulence will be approximately accounted for only in the bulk sense through the Darcy-Weisbach relationship and from friction loss through pipe bends and other components. Figure 1 depicts the control volume used in the development of the governing elastic flow equations.

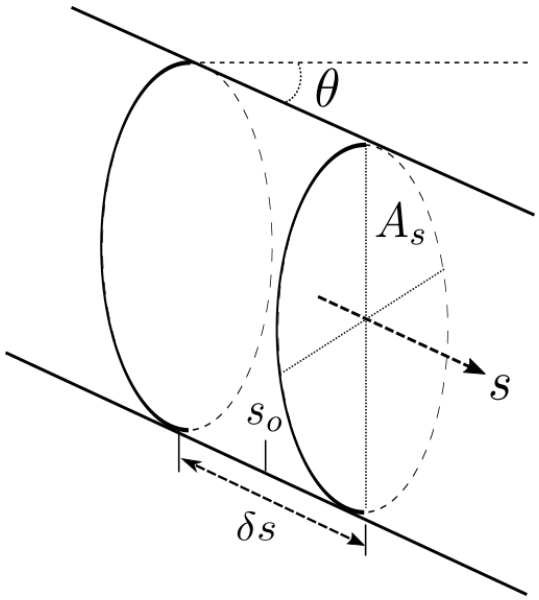

Figure 1. An infinitesimal control volume with length δs, centered at s_o. A_s is the flow area as a function of s. θ is the angle of the pipe, relative to horizontal.

1.1 CONSERVATION OF MASS

For the fixed, nondeforming control volume shown in Figure 1, the conservation of mass for this volume is given by Eq. 1.

$$\frac{\partial}{\partial t}\int \rho dV + \int \rho(v_s \cdot \hat{n})dA = 0 \ , \tag{1}$$

where v_s is the velocity in the direction of the penstock centerline. We can write the boundary integral portion:

$$\int \rho(v_s \cdot \hat{n})dA = (\rho v_s A_s)\Big|_{s_o+\delta s/2} - (\rho v_s A_s)\Big|_{s_o-\delta s/2} \ . \tag{2}$$

Since the volume has infinitesimal size in the direction along the penstock, δs, it useful to re-express the terms on the right-hand side as a Taylor series, and so long as the distance δs is infinitely small, ignore higher order terms in the series:

$$(\rho v_s A_s)\Big|_{s_o+\delta s/2} = \rho_o v_{s,o} A_o + \frac{\partial(\rho v_s A_s)}{\partial s}\frac{\delta s}{2} + \text{H.O.T....} \tag{3}$$

$$(\rho v_s A_s)\Big|_{s_o-\delta s/2} = \rho_o v_{s,o} A_o - \frac{\partial(\rho v_s A_s)}{\partial s}\frac{\delta s}{2} + \text{H.O.T....}$$

$$\int \rho(v_s \cdot \hat{n}) dA = \left[\rho_o v_{s,o} A_o + \frac{\partial(\rho v_s A_s)}{\partial s}\frac{\delta s}{2}\right] - \left[\rho_o v_{s,o} A_o - \frac{\partial(\rho v_s A_s)}{\partial s}\frac{\delta s}{2}\right] \quad . \tag{4}$$

$$= 2\frac{\partial(\rho v_s A_s)}{\partial s}\frac{\delta s}{2} = \frac{\partial(\rho v_s A_s)}{\partial s}\delta s$$

The time derivative term is treated in a similar way:

$$\frac{\partial}{\partial t}\left[\int \rho dV\right] = \frac{\partial}{\partial t}\left[\int \rho A_s ds\right] \quad . \tag{5}$$

And for the infinitesimal volume we obtain

$$\frac{\partial}{\partial t}\left[\int \rho A_s ds\right] = \delta s \frac{\partial(\rho A_s)}{\partial t} \quad . \tag{6}$$

After collecting terms, Eq. 1 becomes

$$\delta s \frac{\partial(\rho A_s)}{\partial t} + \delta s \frac{\partial(\rho v_s A_s)}{\partial s} = 0 \quad . \tag{7}$$

Thus far, we have only transformed the integral form of continuity into a differential form; however, we can use a relationship derived in Section 1.3.1 to greatly simplify the mass balance equation. Furthermore, we can use a magnitude of terms analysis to justify eliminating a term that will remain relatively small under low Mach flow ($v_s << a$).

Note that the density, $\rho(s,t)$, velocity, $v_s(s,t)$, and area, $A_s(s,t)$, are all functions of space, s, and time, t, in the elastic flow case. The product rule is applied to each term in Eq. 7, giving

$$\frac{\partial(\rho A_s)}{\partial t} = A_s \frac{\partial \rho}{\partial t} + \rho \frac{\partial A_s}{\partial t} \quad , \tag{8}$$

and

$$\frac{\partial(\rho v_s A_s)}{\partial s} = v_s A_s \frac{\partial \rho}{\partial s} + v_s \rho \frac{\partial A_s}{\partial s} + A_s \rho \frac{\partial v_s}{\partial s} \quad . \tag{9}$$

Collecting terms yields

$$A_s \frac{\partial \rho}{\partial t} + \rho \frac{\partial A_s}{\partial t} + v_s A_s \frac{\partial \rho}{\partial s} + v_s \rho \frac{\partial A_s}{\partial s} + A_s \rho \frac{\partial v_s}{\partial s} = 0 \quad , \tag{10}$$

or

$$A_s\left[\frac{\partial \rho}{\partial t} + v_s \frac{\partial \rho}{\partial s}\right] + \rho\left[\frac{\partial A_s}{\partial t} + v_s \frac{\partial A_s}{\partial s}\right] + \rho A_s \frac{\partial v_s}{\partial s} = 0 \quad .$$

Now applying the definition of the material derivative in one dimension,

$$\frac{D(\phi)}{Dt} = \frac{\partial \phi}{\partial t}\frac{\partial t}{\partial t} + \frac{\partial \phi}{\partial s}\frac{\partial s}{\partial t} = \frac{\partial \phi}{\partial t} + \frac{\partial \phi}{\partial s} v_s \quad . \tag{11}$$

After applying the material derivative and dividing through by the area and density we obtain

$$\frac{1}{\rho}\frac{D\rho}{Dt} + \frac{1}{A_s}\frac{DA_s}{Dt} + \frac{\partial v_s}{\partial s} = 0 \quad . \tag{12}$$

Next, we make use of the closure models describing the area and density as functions of pressure, ($A_s(p)$ and $\rho(p)$), as given by Eqs. 29 and 24, respectively. By the chain rule, the total derivatives become

$$\frac{D\rho(p)}{Dt} = \frac{\partial\rho(p)}{\partial p}\frac{\partial p}{\partial t}\frac{\partial t}{\partial t} + \frac{\partial\rho(p)}{\partial p}\frac{\partial p}{\partial s}\frac{\partial s}{\partial t} = \frac{\partial\rho}{\partial p}\frac{Dp}{Dt} \ , \text{ and}$$

$$\frac{DA_s(p)}{Dt} = \frac{\partial A_s}{\partial p}\frac{Dp}{Dt} \ .$$

Substituting these into Eq. 12 gives

$$\frac{\partial\rho}{\partial p}\frac{Dp}{Dt} + \frac{\rho}{A_s}\frac{\partial A_s}{\partial p}\frac{Dp}{Dt} + \rho\frac{\partial v_s}{\partial s} = 0 \ . \tag{13}$$

Next, we can use the wave speed definition derived in Section 1.3.1 to simplify the equation further. By substituting Eq. 35 into Eq. 13 and expanding the total derivative of pressure, we obtain

$$\frac{\partial p}{\partial t} + v_s\frac{\partial p}{\partial s} + \rho a^2\frac{\partial v_s}{\partial s} = 0 \ , \tag{14}$$

where a is the local wave celerity. Note that the celerity is a function of the local density of water and pipe cross-sectional area. For 1D flow, note the relationship between the flow velocity, mass flow rate, q, cross-sectional flow area, and water density:

$$v_s = q/(\rho A_s) \ . \tag{15}$$

Using 15 in Eq. 14 gives the conservative form of the continuity equation:

$$\frac{\partial p}{\partial t} + v_s\frac{\partial p}{\partial s} + \rho a^2\frac{\partial(q/(\rho A_s))}{\partial s} = \frac{\partial p}{\partial t} + v_s\frac{\partial p}{\partial s} + \rho a^2\left[\frac{1}{\rho A_s}\frac{\partial q}{\partial s} + \frac{q}{A_s}\frac{\partial(1/\rho)}{\partial s} + \frac{q}{\rho}\frac{\partial(1/A_s)}{\partial s}\right] = 0 \ . \tag{16}$$

Noting that $\partial(1/\rho)/\partial s$ and $\partial(1/A_s)/\partial s$ are small for the hydropower system because of very small density and pipe cross-sectional area changes relative to spatial changes in p and q, we can ignore the last two terms to obtain

$$\frac{\partial p}{\partial t} + v_s\frac{\partial p}{\partial s} + \frac{a^2}{A_s}\frac{\partial q}{\partial s} = 0 \ . \tag{17}$$

And for $v_s << a$,

$$\boxed{\frac{\partial p}{\partial t} + \frac{a^2}{A_s}\frac{\partial q}{\partial s} = 0 \ .} \tag{18}$$

This is the classical conservation of mass equation for elastic flow through a pipe, and an equivalent form is derived in the literature (Chaudhry [2014]). For an example application of the conservative form of the equation written in terms of the mass flow rate, q, see the work by Szydłowski [2002] who also applies the finite volume method to this formulation of this mass conservation equation for elastic flow.

1.2 NEWTON'S SECOND LAW

Next, Newton's second law is applied to the infinitesimal fluid volume in Figure 1, and an expression of the balance of forces acting on the fluid volume element is obtained:

$$\frac{\partial}{\partial t}\int v_s\rho dV + \int v_s\rho(v_s\cdot\hat{n})dA = \sum F \ . \tag{19}$$

After a similar Taylor series expansion procedure and algebraic manipulation, as was done in the mass balance PDE derivation, and accounting for all forces including wall shear, pressure, and inertial effects, and combining Eq. 15 with Eq. 19, Newton's second law gives

$$\boxed{\frac{\partial q}{\partial t} + \frac{\partial \left[q^2/(\rho A_s)\right]}{\partial s} + \frac{\partial (pA_s)}{\partial s} + \rho g A_s \sin(\theta) - \frac{fq|q|}{2\rho A_s D} - S_T - S_m = 0 \ ,} \tag{20}$$

where S_T is the loss from flow through the turbine. S_T is zero, except at the location of the turbine. S_m is minor flow losses through pipe bends, the inlet, and valves. S_m is zero, except at the location of these components. f is the Darcy friction factor and is given by Colebrook formula shown in Eq. 21.

$$\frac{1}{\sqrt{f}} = -2\log\left(\frac{\epsilon/D}{3.7} + \frac{2.51}{\mathrm{Re}\sqrt{f}}\right) \ , \tag{21}$$

which is a transcendental equation that can be solved using fixed-point iteration to obtain f given the pipe roughness, ϵ, and diameter, D, and Reynolds number, $\mathrm{Re} = \frac{\rho v_s D}{\mu}$, which depends on the flow rate. For $\mathrm{Re} < 2000$, indicating laminar flow, f is given by

$$f = \frac{64}{Re} \ . \tag{22}$$

For the minor losses, $S_m = A_s \Delta p / \Delta s$, where the pressure loss value is computed by

$$\Delta p = K_L \frac{1}{2} \rho v_s^2 \ . \tag{23}$$

With the valve loss coefficient, K_L, determined by the valve's geometry and open fraction. Various valve coefficients are available for different valve types and geometries in the literature (Muson et al. [2009]). K_L values for the components included in the hydropower system model under consideration are provided in Chapter 3.

1.3 EQUATION OF STATE AND WAVE SPEED

Closure models are needed to make the solution to the governing PDEs possible since the number of unknown system variables must be equal to the number of equations. The density of water, for instance, must be written in terms of these system variables, (p, q). This leads to the so-called closure relationships, two of which are employed in the elastic flow model: one for the water density and one for the cross-sectional flow area of the pipe.

In the elastic flow model, the density of the water is assumed to depend only on the pressure. In this model, we assume the density of water varies linearly with pressure. The equation of state is given by Eq. 24:

$$\boxed{\rho(p) = \rho_o + \rho_o (p - p_o)/E_{H_2O}} \ , \tag{24}$$

where E_{H_2O} is the Young's modulus of water and is taken to be $\approx 1e9[Pa]$.

The static pressure within the penstock is related to the hoop stress in the penstock pipe wall, as shown by Eq. 25:

$$\sigma_h = \frac{pD}{2e} \ , \tag{25}$$

where p is the static pressure, D is the pipe diameter, e is the pipe wall thickness, and σ_h is the hoop stress. A small increment in pressure $p - p_o$, where p_o is taken to be the atmospheric pressure of 1 atm, results in a corresponding small increment in hoop stress if the pressure change is not so large as to cause plastic deformation in the material:

$$\delta\sigma_h = \frac{(p - p_o)D}{2e} \quad . \tag{26}$$

The hoop stress is related to the strain by Eq. 27:

$$\delta\epsilon = \frac{\delta\sigma_h}{E_p} \quad , \tag{27}$$

where $\delta\epsilon = \delta D/D_o = (D - D_o)/D_o = D/D_o - 1$ is the strain and $E_p \approx 1e11[Pa]$ is Young's modulus of the pipe wall. The pipe flow area is $A = \pi D^2/4$. Combining Eqs. 26 and 27 results in

$$\begin{aligned} D &= D_o\left(\frac{(p - p_o)D}{2E_p e}\right) + D_o \\ D\left[1 - D_o\left(\frac{(p - p_o)}{2E_p e}\right)\right] &= D_o \\ D &= D_o\left[1 - D_o\left(\frac{(p - p_o)}{2E_p e}\right)\right]^{-1} \quad , \end{aligned} \tag{28}$$

and rewriting in terms of the area gives an expression for the pressure-dependent pipe cross sectional area:

$$\boxed{A(p) = \frac{\pi}{4}\left[D_o\left(\frac{(p - p_o)D}{2E_p e}\right) + D_o\right]^2} \quad . \tag{29}$$

1.3.1 Wave Speed

A pressure wave propagates in an elastic medium with speed, a, given by Eq. 30, assuming the wave's compression and rarefaction are reversible (a constant entropy process).

$$\frac{1}{a^2} = \frac{d\rho}{dp} \quad , \tag{30}$$

so for an idealized case, $a = \sqrt{\frac{dp}{d\rho}}$. However, since the area of the pipe changes as a function of pressure, the original wave speed can be modified to include the impact of the elastic pipe. This has the effect of slightly decreasing the effective wave speed through the penstock system. Consider the density of water that is required to fill a changing pipe segment volume, δV, where the pipe is allowed to change its diameter only but not its length; this allows us to write

$$\delta V = \delta A_s \Delta x \quad .$$

Ignoring other effects, the density of water can be expressed as a function of the pipe flow area, and the area as a function of pressure; therefore,

$$\rho(A(p)) = \frac{m_o}{A(p)\Delta x} = \frac{\rho_o A_o \Delta x}{A(p)\Delta x} = \frac{\rho_o A_o}{A(p)} \quad .$$

Then, by the chain rule, the sensitivity of the density with respect to pressure is

$$\left.\frac{\partial \rho}{\partial p}\right|_{p_o} = \left.\frac{d\rho}{dA}\right|_{A(p_o)} \left.\frac{dA}{dp}\right|_{p_o}$$

or

$$\left.\frac{\partial \rho}{\partial p}\right|_{p_o} = \frac{-\rho_o A_o}{A_o^2}\frac{dA}{dp} = \frac{-\rho_o}{A_o}\frac{dA}{dp} \quad .$$

An expression for the sensitivity of the pipe cross-sectional area to the pressure is given by Gale and Tiselj [2002], as originally was given by Wylie and Streeter [1978]:

$$\frac{dA_s}{A_s} = \frac{D}{e}\frac{dp}{E_p} = K dp \quad . \tag{31}$$

Rearranging terms gives

$$\frac{1}{A_s}\frac{dA_s}{dp} = K \quad , \tag{32}$$

and Gale and Tiselj [2002] state that

$$\frac{1}{a^2} = \frac{1}{a_o^2} + K\rho \quad ; \tag{33}$$

therefore,

$$\frac{1}{a^2} = \frac{1}{a_o^2} + \frac{\rho}{A_s}\frac{dA_s}{dp} \quad , \tag{34}$$

where a_o is the speed of sound in a pure unbounded liquid and in the ideal case $a_o = \sqrt{\frac{dp}{d\rho}}$.

This leads to an expression for the wave speed in an elastic pipe:

$$\frac{1}{a^2} = \frac{d\rho}{dp} + \frac{\rho}{A}\frac{dA}{dp} \quad . \tag{35}$$

This expression is also useful to simplify the mass balance shown in Eq. 13.

1.3.2 Vectorized Conservation Law Form

Briefly, we restate the conservation of mass and Newton's second law into a vectorized format to facilitate the application of the finite volume method to the PDEs. A few useful definitions are as follows:

q = mass flow rate in [kg/s].

p = static pressure in [Pa].

ρ = density in [kg/m^3].

a = wave speed in [m/s].

A_s = pipe cross-sectional area in [m^2].

D = pipe inner diameter in [m].

The final mass and momentum equations can be expressed in the vector form:

$$\frac{\partial}{\partial t}\begin{bmatrix} p \\ q \end{bmatrix} + \begin{bmatrix} \frac{a^2}{A_s} & 0 \\ 0 & 1 \end{bmatrix}\left[\frac{\partial}{\partial s}\begin{bmatrix} q \\ \frac{q^2}{\rho A_s} + pA_s \end{bmatrix}\right] + \begin{bmatrix} 0 \\ -\rho g A_s \sin(\theta) + \frac{fq|q|}{2\rho A_s D} \end{bmatrix} = \begin{bmatrix} 0 \\ 0 \end{bmatrix} \ , \tag{36}$$

which can be written in the compact form:

$$\frac{\partial U}{\partial t} + B\frac{\partial F(U)}{\partial s} + S = 0 \ , \tag{37}$$

where

$$U = \begin{pmatrix} p \\ q \end{pmatrix}$$

$$B = \begin{pmatrix} a^2/A_s & 0 \\ 0 & 1 \end{pmatrix}$$

$$F = \begin{pmatrix} q \\ \frac{q^2}{\rho A_s} + pA_s \end{pmatrix}$$

$$S = \begin{pmatrix} 0 \\ -\rho g A_s \sin(\theta) + \frac{fq|q|}{2\rho A_s D} \end{pmatrix} \ .$$

1.4 FINITE VOLUME DISCRETIZATION AND SOLUTION PROCEDURE

Using a finite volume approach, we begin by integrating Eq. 37 over an interior cell:

$$\int \frac{\partial U}{\partial t} dV + \int B\frac{\partial F(U)}{\partial s} dV + \int S\, dV = 0 \ . \tag{38}$$

Using the divergence theorem we obtain

$$\int \frac{\partial U}{\partial t} dV + \int BF \cdot \hat{n} dS - \int F(\nabla \cdot B) dV + \int S\, dV = 0 \ . \tag{39}$$

Note that if a is taken to be a constant then $\nabla \cdot B = 0$; but for nonconstant wave speed models, this term cannot be neglected and is an additional volume source term. This source term will be neglected in the following discussion of the discretization scheme as it can be treated similarly to the source, S. For the 1D finite volume discretization shown in Figure 2, for an interior cell with index i and with cell boundary faces indexed by $i + 1/2$ and $i - 1/2$, respectively, the surface integrals can be replaced by their discrete representation:

$$\int \frac{\partial U_i}{\partial t} dV + \left[BF_{i+1/2}A_{s,i+1/2} - BF_{i-1/2}A_{s,i-1/2}\right] + S_i V_i = 0 \ , \tag{40}$$

where the cell volume is given by $V_i = \int A_s ds_i$.

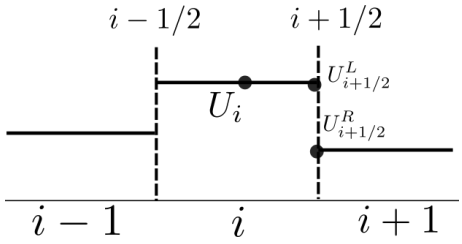

Figure 2. Finite volume mesh.

To solve this semidiscrete system, we treat the volume source term(s) separately from the advection term. The idea is to separately compute the individual contribution of each term to the time rate of change of the conserved quantities and then sum their effects as a final step. This would be analogous to operator splitting if there were a diffusion term. The computation of the interface cell fluxes, specifically the evaluation of $F_{i+1/2}$ and $F_{i-1/2}$, is the focus of the next section.

1.4.1 The Riemann Problem

Consider the homogeneous form

$$\frac{\partial U}{\partial t} + \frac{\partial F(U)}{\partial s} = 0 \ , \tag{41}$$

which can be rewritten as

$$\frac{\partial U}{\partial t} + \frac{\partial F}{\partial U} \cdot \frac{\partial U}{\partial s} = 0 \ ,$$

with initial conditions

$$U(s, t = 0) = \begin{cases} U_L & s \leq 0 \\ U_R & s > 0 \end{cases} .$$

Equation 41, along with the stated initial conditions, is known as the Riemann problem, which is a specific initial value problem relevant to transport problems. This problem arises in compressible flow, where a shock might form a discontinuity in the solution variable, and the solution to the Riemann problem dictates how the shock propagates. This problem arises, in general, in the solution of linear hyperbolic systems (and nonlinear systems that are linearized) on cell-centered finite volume meshes.

We can rewrite the advection-driven component of the elastic flow problem at hand into the format of the standard Riemann problem. First, the chain rule can be applied to the first-order space derivative term; since $F = F(U(s, t))$, we can write

$$B\frac{\partial F(U)}{\partial s} = B\frac{\partial F}{\partial U} \cdot \frac{\partial U}{\partial s} = BJ \cdot \frac{\partial U}{\partial s} = A \cdot \frac{\partial U}{\partial s} \ , \tag{42}$$

where $J = \frac{\partial F}{\partial U}$ is the Jacobian of F and $A = BJ$.

$$J = \begin{pmatrix} 0 & 1 \\ A_s & \frac{2q}{\rho A_s} \end{pmatrix} \tag{43}$$

$$A = BJ = \begin{pmatrix} 0 & \frac{a^2}{A_s} \\ A_s & \frac{2q}{\rho A_s} \end{pmatrix} \ . \tag{44}$$

Considering the advection term only, Eq. 37 can be simplified as

$$\frac{\partial U}{\partial t} + A \cdot \frac{\partial U}{\partial s} = 0 \ . \tag{45}$$

1.4.2 Approximate Solution to the Riemann Problem

The exact solution to the Riemann problem is not computationally feasible in many scenarios since, in general, this requires exactly solving a system of nonlinear equations (for instance A is nonlinear, as is the present case since a and A_s are a function of p). Rather than exactly solving the problem, it is possible to obtain an approximate solution to the Riemann problem with significantly less computational effort. This is desirable for the real-time application of the hydropower digital twin.

Solutions to the Riemann problem have been studied extensively by the compressible flow community, and landmark works by Roe [1981], and later by others, give many strategies for approximately solving this equation on cell-centered finite volume meshes.

The KT central scheme was selected for this work for its simplicity and relative accuracy compared with other approximate Riemann solver solution methods (Kurganov and Tadmor [2000]). The KT scheme gives an approximate solution for the numerical flux across a finite volume cell boundary by

$$F_{i+1/2} = \frac{F_L^{i+1/2} + F_R^{i+1/2}}{2} - \frac{a(A|_{L,R}^{i+1/2})}{2}\left(U_R^{i+1/2} - U_L^{i+1/2}\right) \ , \tag{46}$$

where $a(A|_{L,R}^{i+1/2})$ is the maximum spectral radius of the Jacobian evaluated at the $i + 1/2$ interface on the left and right sides of the interface:

$$a(A|_{L,R}^{i+1/2}) = \max\left[\rho(A_L^{i+1/2}), \rho(A_R^{i+1/2})\right] \ , \tag{47}$$

where $U_L^{i+1/2}$ and $U_R^{i+1/2}$ are the left and right values of the solution fields, $[p, q]$, at the cell interface $i + 1/2$. These values are computed by extrapolating cell-centered values, U_i, to the cell interfaces using the MUSCL scheme (discussed in Section 1.4.3). Here, $\rho(A)$ is the spectral radius of A. The computation of the spectral radius of the Jacobian at each finite volume cell interface is numerically the most expensive portion of the elastic flow solver used in this work. This requires computation of the eigenvalues of the Jacobian, which for a 2×2 matrix can be done analytically and quickly. Note that for systems with a larger number of solution variables, such as in two-phase flow applications, the KT scheme in its semidiscrete form as shown here is more challenging to apply in a numerically efficient manner.

By the KT method, the approximate solution to the initial value problem given by Eq. 41 can be formed from the aforementioned numerical fluxes, $F_{i\pm1/2}$, and by integrating the semidiscrete form shown in Eq. 48 using an appropriate time integration strategy such as a Runge-Kutta method.

$$\frac{dU_i}{dt} = -\frac{F_{i+1/2} - F_{i-1/2}}{\Delta s} \ . \tag{48}$$

1.4.3 Extrapolating Cell-Centered Values to Faces by MUSCL Reconstruction

The face values $U_{L,R}^{i\pm1/2}$ are computed by MUSCL (Van Leer [1974]). A generalized form of the MUSCL scheme is given in Eq. 49.

$$u_L^{i+1/2} = u_i + \frac{\phi}{4}\left[(1-\kappa)\psi\left(\frac{u_{i+1} - u_i}{u_i - u_{i-1}}\right)(u_i - u_{i-1}) + (1+\kappa)\psi\left(\frac{u_i - u_{i-1}}{u_{i+1} - u_i}\right)(u_{i+1} - u_i)\right] \ , \tag{49}$$

where $\kappa \in [-1, 1]$ and $\phi \in \{0, 1\}$ are parameters of the generalized MUSCL scheme, with $\kappa = 1/3$ and $\phi = 1$ used in this work. κ controls the amount of upwind or downwind bias in the computation of the interface values. ϕ is either a 0 or 1 and controls the order of accuracy of the reconstruction, with 0 yielding a piecewise constant reconstruction and $\phi = 1$ giving a piecewise linear reconstruction, which improves the estimates for the interface values. ψ is a flux limiter function. The superbee limiter is given by (Arora and Roe [1997]):

$$\psi(r) = \max(0, \min(1, 2r), \min(r, 2)) \quad . \tag{50}$$

The limiter function prevents introducing artificial extrema in the solution approximation, which would result in increasing error and instability.

Note that in Eq. 49 to reconstruct a piecewise linear approximator to the interface values the MUSCL scheme requires cell values to the left, U_{i-1}, and right, U_{i+1}, of any given cell; however, these quantities exist only for interior cells. 1D finite volume cells on the boundary have only one neighbor. To avoid accuracy issues at the boundary cells, ghost cells are introduced at the boundaries, which are used to enforce boundary conditions. The ghost cells are not a part of the interior solution domain. A small test problem was constructed to qualitatively show the influence of ϕ and choice of ψ on the MUSCL scheme's capability to represent smooth and discontinuous portions of a solution field. Shown in Figures 3 and 4, a piecewise quadratic function with a discontinuity at $s = 50$ was used to test the MUSCL scheme with the form:

$$U = \begin{cases} (50 - s)^2 + 2550 & s \leq 50 \\ -(50 - s)^2 - 2550 & s > 50 \end{cases} \quad .$$

Figure 4 shows that the superbee and Van Albada 1 limiters prevent forming artificial extrema in the reconstruction near the discontinuity. The Van Albada 1 limiter has the form $\psi(r) = (r^2 + r)/(r^2 + 1)$ (Van Albada et al. [1982]). Compared to the superbee limiter, the Van Albada limiter gives a slightly better fit to the test function near the discontinuity in this specific case. Both limiters are implemented in the elastic flow model and can be selected at runtime. The superbee limiter was used in all elastic flow model computations presented in this report.

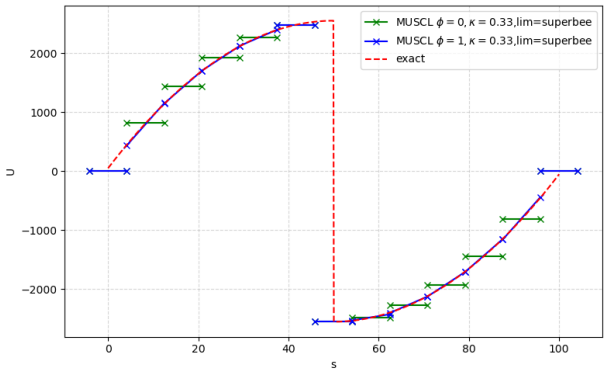

Figure 3. MUSCL scheme with different values of ϕ.

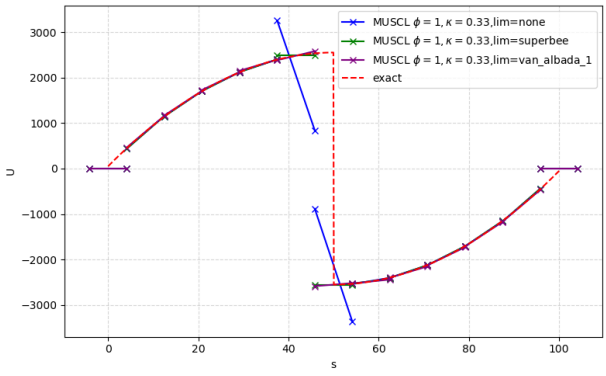

Figure 4. MUSCL scheme with different flux limiters.

1.4.4 Time Integration

The final term remaining is the time derivative. After application of the KT scheme to the advection terms, what is left is a series of ordinary differential equations (ODEs) for each finite volume element that can be stepped forward in time. The time integration is performed by the midpoint method.

From Eq. 40, a single finite volume element where the solution is piecewise constant in each volume in the mesh reveals that

$$\frac{\partial U_i}{\partial t} \int A_s ds_i + \left[BF_{i+1/2}A_{s,i+1/2} - BF_{i-1/2}A_{s,i-1/2}\right] + S_i V_i = 0 \ , \tag{51}$$

where $\int A_s ds_i$ represents the volume of the i^{th} element in the finite volume mesh, V_i, accounting for nonconstant pipe diameter.

$$\frac{\partial U_i}{\partial t} = \frac{-1}{V_i}\left[(BF_{i+1/2}A_{s,i+1/2} - BF_{i-1/2}A_{s,i-1/2}) + S_i V_i\right] \ . \tag{52}$$

Let:

$$X_i = \frac{\partial U_i}{\partial t} \ . \tag{53}$$

By the midpoint method, with time step size, Δt:

$$\begin{aligned} U^p &= U^t + \frac{1}{2}\Delta t X^t \\ U^{t+1} &= U^t + \Delta t X^p \ , \end{aligned} \tag{54}$$

with $X_i^p = \frac{\partial U_i^p}{\partial t}$.

This is a second-order explicit time integration method and imposes requirements on the maximum time step size to maintain stability. In practice, since the wave celerity is large for the hydropower penstock system ($a \approx 1000[m/s]$), if the mesh step size is $\Delta x \approx 1[m]$, the time step size must be on the order of $\Delta t \approx 0.001[s]$ to ensure the Courant–Friedrichs–Lewy condition is met: $(\Delta t \sqrt{a^2 + v_s^2})/\Delta x < 1$. This makes the real-time execution of the model challenging, since 1,000 steps must be taken to advance the simulation time by 1 s. Each step requires many 2×2 matrix eigenvalue computations to obtain the requisite local wave speed needed to obtain the fluxes across each cell interface in the KT scheme.

2. TURBINE DYNAMIC MODEL

The Francis turbine design is the focus of the present work. A visual representation of a Francis turbine is given in Figure 5.

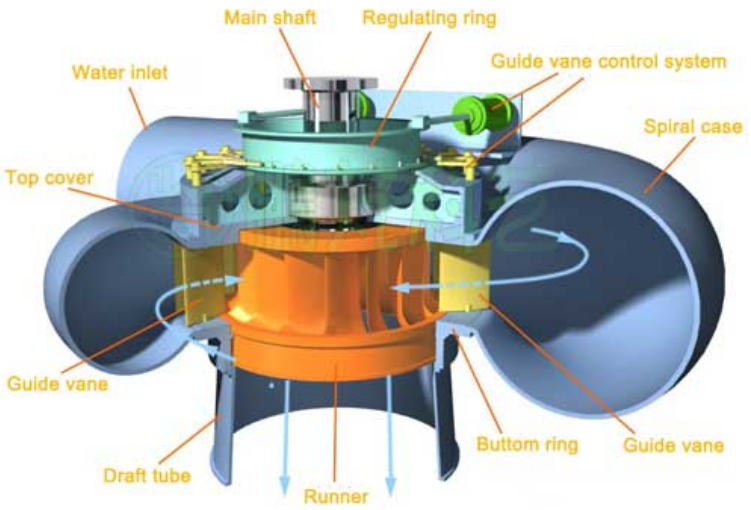

Figure 5. A Francis turbine with key components shown (Vytvytskyi and Lie [2018]).

Here, the inlet guide vane angle, α_1, is considered to be a controllable parameter; under closed-loop control, the vane angle is adjusted to maintain the appropriate rotation rate. Other important aspects of the Francis turbine considered in the following models are the outer radius of the runner, inner runner radius and the height, and angles of the runner blades.

2.1 TORQUE BALANCE

First, a torque balance is written for the turbine runner, shaft, and generator rotor. The moment of inertia of all these spinning components is denoted as J. The angular velocity of the turbine is denoted, ω. Torques applied to the shaft are the following: (1) torque applied by the fluid on the runner vanes as the vanes deflect the flow, T_w, (2) torque applied by bearings from friction losses, T_B, and (3) torque from the generator load, T_L.

$$J\frac{d\omega}{dt} = T_w - T_L - T_B \ . \tag{55}$$

This ODE is coupled to the flow equation through the T_w term, as the torque applied by the flow moving through the turbine depends on the flow rate, among other things.

The load torque, T_L, is assumed to be a known quantity in this report, and it might be a function of time. In reality, the load torque depends on the generator model and grid load. A complete load model and coupling to the power grid is beyond the scope of this report. The friction torque is assumed to follow the simple linear relationship $T_B = b\omega$, where b is a constant and is set to 1, but it could be tuned provided data. The flow torque, T_w, is the most complex term in the torque balance and is computed using conservation of mass and momentum of the flow through the turbine. This torque is reviewed in the following section.

2.2 TURBINE FLOW MODEL

The turbine model developed by Vytvytskyi and Lie [2018] is adopted in this work and is briefly reviewed here. This model relates the flow rate q, vane angle α_1, and rotation rate ω to shaft torque T_w, produced by

the flow of water through the turbine. Furthermore, this model includes a variety of loss terms in the pressure loss formulation, including the effects of friction, shock, and whirl. The model contains several tunable parameters that could be obtained via computational fluid dynamics (CFD) modeling or by experiment.

From the model developed by Vytvytskyi and Lie [2018], the shaft power generated by the flow through the turbine is given by

$$\dot{W}_s = q\omega\left(R_1\frac{\dot{V}}{A_1}\cot(\alpha_1) - R_2\left[\omega R_2 + (\dot{V}/A_2)\cot\beta_2\right]\right) \ , \tag{56}$$

where $\dot{V} = q/\rho$ is the volumetric flow rate, α_1 is the inlet guide vane angle, R_1 is the outer runner radius, R_2 is the inner runner radius, A_1 is the runner inlet flow area, and A_2 is the runner outlet flow area. β_1 is the inlet blade angle, and β_2 is the outlet blade angle.

The torque supplied to the shaft because of the flow is

$$T_w = \dot{W}_s/\omega \ . \tag{57}$$

Equation 57 can be plugged into Eq. 55 to complete the torque balance.

The energy loss from friction is given by

$$\dot{W}_{ft} = k_{ft,1}\dot{V}(\cot\gamma_1 - \cot\beta_1)^2 + k_{ft,2}\dot{V}\cot^2\alpha_2 + k_{ft,3}\dot{V}^2 \ , \tag{58}$$

where $k_{ft,1}$, $k_{ft,2}$, and $k_{ft,3}$ are tunable loss coefficients representing the shock, whirl, and flow friction losses through the turbine, respectively. These coefficients can be determined by Bayesian inference using data collected via experimental means or by executing a series of high-fidelity CFD simulations of the turbine. α_2 can be computed from $\cot(\alpha_2) = \cot(\beta_2) + \omega R_2/(\dot{V}/A_2)$ and $\cot(\gamma_1) = \cot(\alpha_1) - \omega R_1 A_1/\dot{V}$.

The net work rate done by the water on the turbine is

$$\dot{W}_t = \dot{W}_s + \dot{W}_{ft} \ , \tag{59}$$

but only $\dot{W}_s$ is usable work with $\dot{W}_{ft}$ representing losses and inefficiency in the system. The turbine efficiency can be defined as

$$\eta = \frac{\dot{W}_s}{\dot{W}_t} \ . \tag{60}$$

2.3 PID CONTROL OF THE TURBINE

The guide vane angle, α_1, is under closed-loop control in the model. The vane angle is adjusted by a potential, integral, derivative (PID) control scheme to maintain a specified rotation rate of the turbine.

The PID controller is implemented as follows. For each time step, k, the value for the vane angle set point is computed by:

$$\alpha_{1,k} = K_p e_k + K_i\int_0^{t_k} e(\tau)d\tau + K_d\frac{de_k}{dt} \ , \tag{61}$$

where $e_k = \omega_k - \omega_k^*$, with ω^* representing the rotation rate set point. K_p, K_i, and K_d are the potential, integral and derivative gains, respectively, and are constants in the present model.

And because discrete time steps are taken with size, Δt_k, the integral is approximated with the cumulative sum:

$$\int_0^{t_k} e(\tau)d\tau \approx \sum_{i=0}^{k} e_i \Delta t_i = I_k \quad .$$

This is computed using a running sum:

$$I_k = I_{k-1} + \Delta t e_k \quad .$$

And the derivative error term is approximated by finite difference:

$$\frac{de_k}{dt} \approx \frac{e_k - e_{k-1}}{\Delta t_k} \quad .$$

Limits are placed on the minimum and maximum turbine inlet guide vane angle in the model. The minimum possible angle is set to $\alpha_{1,min} = 0.01^o$, and the maximum possible angle is $\alpha_{1,max} = 12^o$. Additionally, when the turbine is under very low load, detected by having a load torque less than $50[kN \cdot m]$, the maximum allowed vane angle is 3^o. This is done to restrict the flow through the turbine under low load to prevent rapid spin-up of the turbine. Furthermore, the maximum rate at which the vane angle is allowed to change is limited to 20^o per second. In reality, this maximum vane movement rate is dictated by the servo system, and depends on the parameters of the machine.

3. RESULTS

The approximate penstock geometry was constructed for a hypothetical, simplified hydroelectric facility. The geometry is consistent with operational hydroelectric units, but the exact dimensions are kept anonymous and general. In the example hydroelectric facility, the total flow path distance between the penstock inlet and outlet to the tailwater is 70.76 m. The simplified geometry used in the model is given in Figure 6. The true draft tube and tailwater geometry is simplified significantly in the present model. Compared with a real-world case, the expansion of the flow area in the true draft and tailwater outlet is not present in the modeled geometry.

The model parameters, such as the assumed pipe roughness and PID gains, are given in Table 1.

The model includes minor pressure losses for the butterfly valve and the discharge to the tailwater. Other minor losses such as the entrance loss, and losses associated with pipe bends were ignored. The inlet loss coefficient for a smooth, rounded inlet is on the order of $K_L \approx 0.04$, whereas, the exit loss coefficient for a pipe discharging to a large body of water is on the order of $K_L \approx 1$ (Muson et al. [2009]). Since the outlet and butterfly valve minor losses dominate the other minor losses within the system, only these two components were included in the model. The loss coefficient for the outlet was taken to be a constant value $K_L = 0.9$. The loss coefficient for the butterfly valve depends on the butterfly valve open fraction, a_b, and is given by $K_L = 0.01 + (0.2/a_b^{1.1})$ where $a_b \in (0, 1]$ and $a_b = 1$ indicates the valve is completely open. Equation 23 is used to compute the pressure loss across these components within the model.

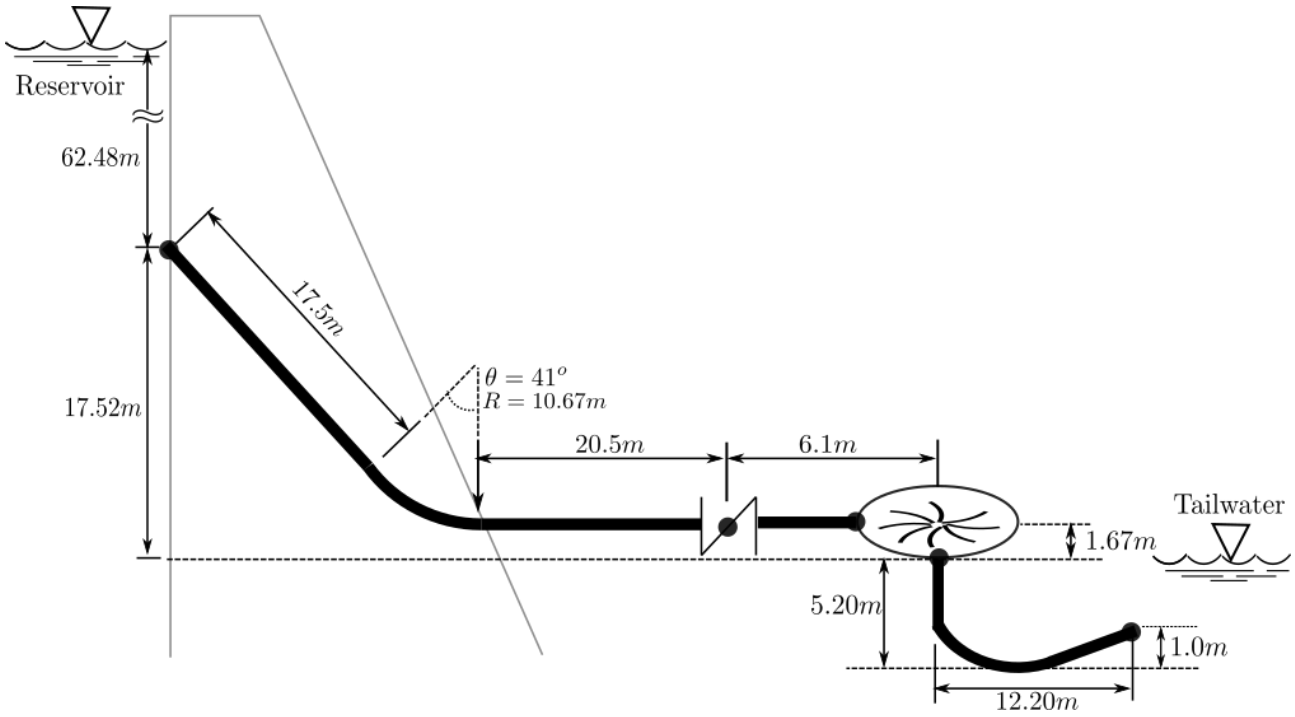

Figure 6. Simplified dam geometry used in flow simulations. Note: not to scale.

Table 1. Model parameters

Parameter	Description	Value	Unit
ϵ	Wall roughness	8.0e-4	(m)
e	Wall thickness	0.04	(m)
D	Penstock inner diameter	3.0	(m)
K_p	PID proportional gain	0.04	(-)
K_i	PID integral gain	0.03	(-)
K_d	PID derivative gain	0.0	(-)

Before running the model, the initial conditions were specified: An initial mass flow rate of 0 kg/s was specified everywhere in the penstock. The initial turbine rotation rate is 0 RPM. The initial pressure profile was computed from the hydrostatic equilibrium condition so that the initial static pressure in each finite volume cell: $p = \rho g h_i$, where h_i is the depth of water of cell i below the reservoir surface.

The following boundary conditions were also used in the example case shown here. The reservoir water height above the tailwater level was held constant at 80 m, which provides the inlet static pressure boundary condition. In the model, the inlet to the penstock is located at approximately 62.5 m below the reservoir water surface. The outlet of the draft tube is located 4.2 m below the surface of the tailwater in the model, so a static head of 4.2 m was specified as the outlet boundary condition. The tailwater level was held fixed in the model throughout the duration of the simulation.

Additional boundary conditions are needed for the coupled turbine model. The grid load, represented as a

known function of time, T_L, is specified. The prespecified load profile as a function of time is given in Figure 7. The model starts with no grid load, ramps to a low load condition, and is then subject to a gradual rise in load up to 900 $kN \cdot m$. Then, at 35 s, the model is subjected to an instantaneous +10% increase in grid load. In reality, this load torque depends on the grid coupling and generator model; however, in the present work the generator and grid coupling is not modeled and instead a simple prespecified load torque profile is used. Additionally, the butterfly valve opening is a known, prespecified function of time. This butterfly valve is opened slowly at the start-up of the machine and in reality is opened after the turbine chamber is flooded with water during the start-up sequence. In the present case, the butterfly valve is initially closed at $t = 0$ s and opens completely by $t = 10$ s. The rate of the valve opening is constant, and the pressure loss through the butterfly valve is given by Eq. 23.

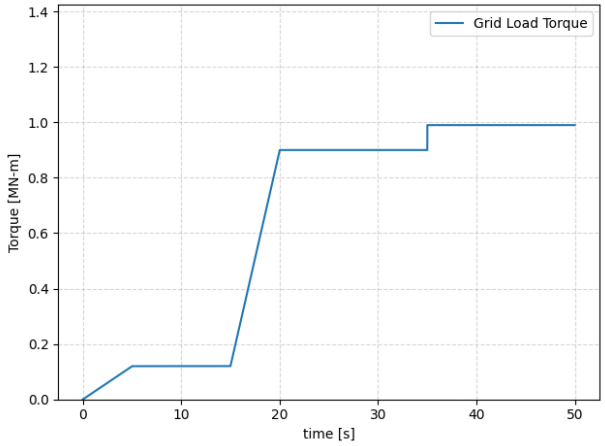

Figure 7. Specified grid load torque profile, T_L, as a function of time.

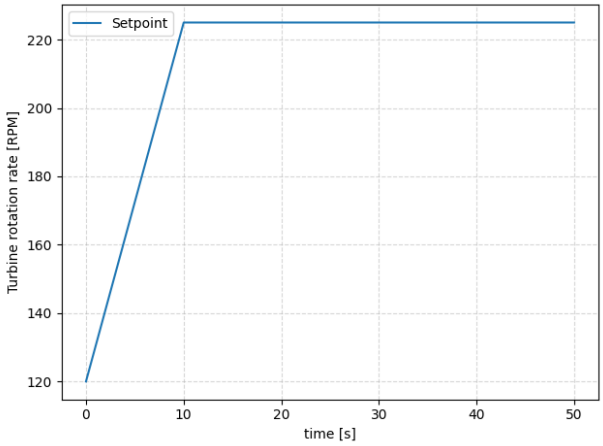

Figure 8. Turbine rotation rate set point, ω^*, as a function of time.

The desired rotation rate of the turbine is also prespecified up-front. The set point schedule for the turbine rotation rate used in this example case is given in Figure 8. The desired steady-state turbine rotation rate is 225 RPM in this case. This rate corresponds to a grid frequency of 60 Hz if the number of pole pairs in the generator is equal to 16: $n = 225 = \frac{60 f_g}{p}$, where $f_g = 60[Hz]$ is the grid frequency and p is the number of pole pairs in the generator.

3.1 ELASTIC MODEL RESULTS

The elastic flow model simulated the start-up transient sequence with the inital and boundary conditions specified in the previous section. The time- and space-dependent volumetric flow rate and gauge static pressure are given in Figures 9 and 10. Qualitatively, the 3D surface figures show the impact of the turbine on the pressure field, seen as a large static pressure drop at position = 55 m in the 3D pressure figure, and the system response to increases in the grid load. Because it is difficult to extract quantitative information from the 3D surface plots, follow-on figures show slices of the fundamentally time- and space-dependent quantities.

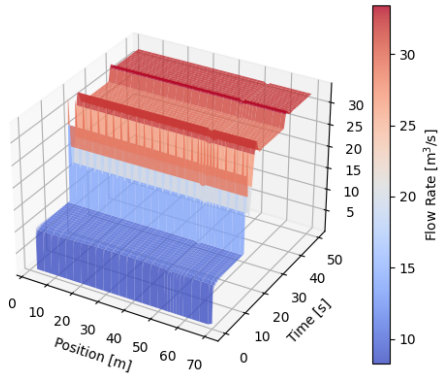

Figure 9. Volumetric flow rate $\dot{V}$ from the elastic flow model as a function of time and space.

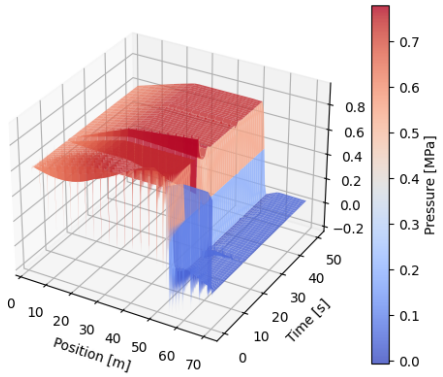

Figure 10. Static gauge pressure from the elastic model as a function of time and space.

Figure 11 gives a snapshot of the static pressure and volumetric flow fields at the end of the simulation period, near t = 50 s. This is the steady-state behavior of the system predicted by the elastic model. The capability to handle varying the mesh size was included the finite volume–based numerical method implementation. The finite volume cell centers are represented as the nodes in the plot so that the mesh spacing can be seen. A refined mesh was used around the turbine and draft tube section of the domain, with a mesh spacing of 0.5725 m. A coarser mesh was used in the penstock section upstream of the turbine with a cell width of 1.45 m. The capability to refine and coarsen the mesh increases the numerical accuracy of the method in sharp pressure gradient regions and reduces the calculation time by coarsening the mesh in other areas. Results from a mesh converge study for a simplified linear advection problem are provided in Appendix A.

The pressure profile, seen as a red line in Figure 11, shows that the model predicts a small negative gauge pressure immediately downstream from the turbine in the draft tube. This indicates a vacuum condition at this location and is consistent with the expected operation. If the absolute static pressure (gauge pressure + 101.3 kPa) locally drops below the vapor pressure, or about 3,000 Pa at 25°C, cavitation is likely. The dotted horizontal line in figure 11 is drawn at this cavitation pressure threshold. In this case, the bulk gauge pressure does not drop below this value; however, extremely fine 3D local pressures are not captured by the 1D elastic flow model and would require a CFD analysis to obtain estimates for localized cavitation at the trailing edge of the runner blades. Localized cavitation on the training edge of the turbine is known to contribute to erosion and degradation of turbine performance (Gordon [1992]); however, it is beyond the scope of the 1D model to produce such estimates at this time. Future work could investigate coupling localized cavitation and blade degradation models with the elastic flow model developed here to achieve a multi-scale modeling of the turbine erosion physics.

The turbine inlet gauge static pressure—as measured at the shell casing inlet upstream from the guide vanes—predicted by the elastic flow model is presented in Figure 12. Some hydroelectric facilities actively monitor penstock and turbine inlet pressures using piezoelectric static pressure sensors, so the model predicted turbine inlet pressure results can be a useful point of comparison and used for model calibration activities.

At steady state, at t=50 s, the turbine inlet static gauge pressure was predicted to be 745,770 Pa or 108.16 psig. This turbine inlet static pressure can be converted to static head by dividing through by a factor of ρg. After start-up from t = 0 to t = 8 s, large pressure oscillations are predicted by the model as the flow stabilizes as the butterfly valve opens completely. At t = 15 s, the load is increased rapidly, and the model predicts a large pressure transient that corresponds to rapid changes in the inlet guide vane angle needed to meet the load increase. The magnitude of the pressure swings present in figure 12 partially depend on the rate and magnitude of the inlet guide vane angle changes. Figure 13 shows that the power ramp transient beginning at t=15 s results in a faster increase in the vane angle compared to the transient at t=35 s. This is due to the vane angle being initially limited to 3^o prior to 15s due to a low load condition followed by a rapid lift of the max allowed vane angle to 12^o after the low load condition is overcome. Together, the PID controller and simplified servo model dictate the rate of vane movement.

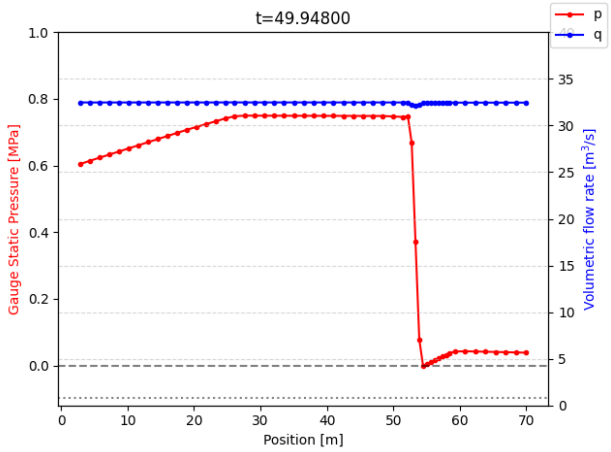

Figure 11. Volumetric flow rate and static gauge pressure distribution at time t = 49.948 s.

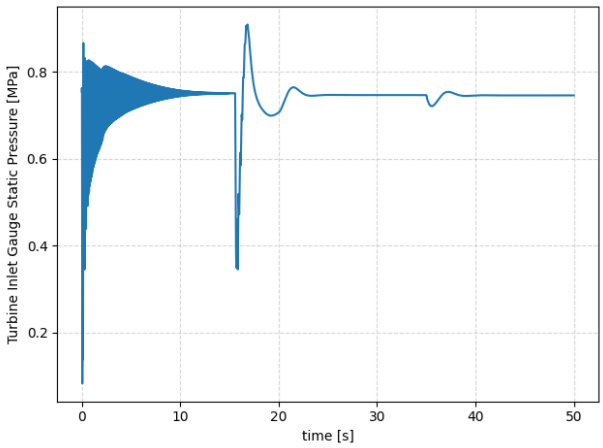

Figure 12. Static gauge pressure at the turbine inlet as a function of time.

Figure 13 shows the performance of the PID controller as the inlet guide vane angle, α_1, is adjusted by the PID controller to maintain the set point rotation rate shown in Figure 16. Initially, the controller is limited to a maximum vane open angle of only 3^o under low-load conditions from t = 0 to t =15 s. This is to prevent rapid spin-up of the turbine. However, after t = 15 s, the maximum allowed vane angle is lifted to 12^o since the load is above the low-load threshold. At this time, the PID controller rapidly opens the inlet vane angle to allow more flow through the turbine to quickly achieve the set point of 225 RPM. After the +10% load change at 35 s of operation, the PID controller adjusts the vane angle to approximately 10^o. At this time, the predicted total power produced by the turbine is 25 MW, as shown in Figure 15, and as shown in figure 14 the shaft torque produced by the turbine at this time is 1 MN-m.

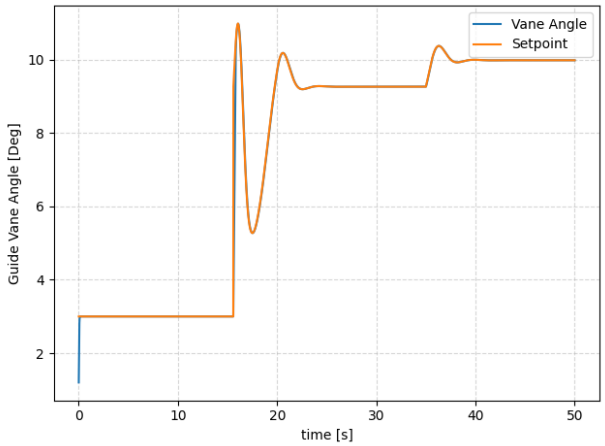

Figure 13. Turbine inlet vane angle vs. time. The set point is from the PID control signal.

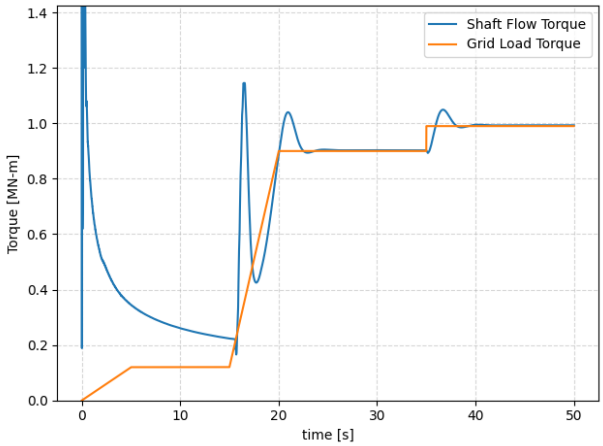

Figure 14. Applied load T_L and shaft torque T_w due to water flow.

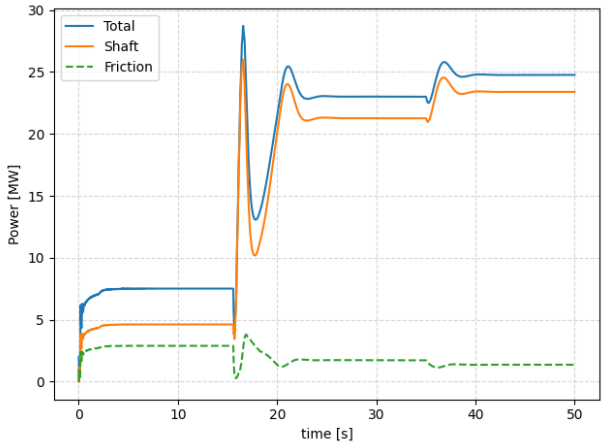

Figure 15. Turbine power as a function of time.

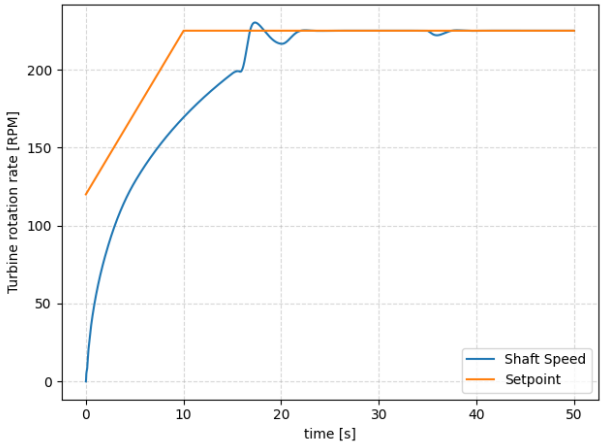

Figure 16. Turbine rotation rate vs. time.

The elastic flow model predictions for the volumetric flow rate through the turbine are presented in Figure 18. From $t = 0$ to 15 s, the inlet vane angle was restricted to a maximum opening of 3^o and so restricted the flow rate considerably under the low-load conditions encountered in the start-up sequence. With the guide vane opening of 10^o, seen in Figure 13, the final steady-state flow rate through the turbine at 50 s, was 32.184 m^3/s. In the simulation, the guide vane opening position was determined by the PID controller such that the set point rotation rate is maintained under a given load.

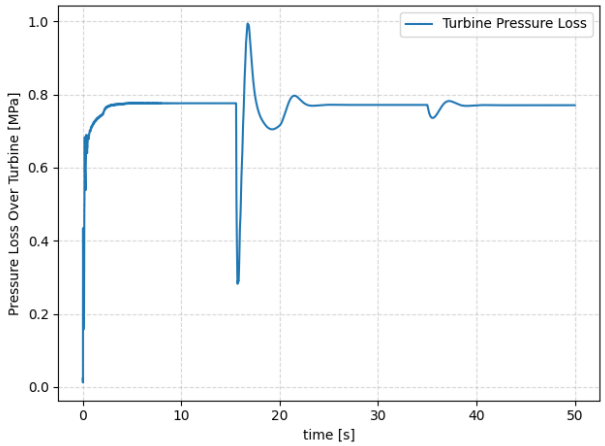

Figure 17. Static Δp over the turbine as a function of time.

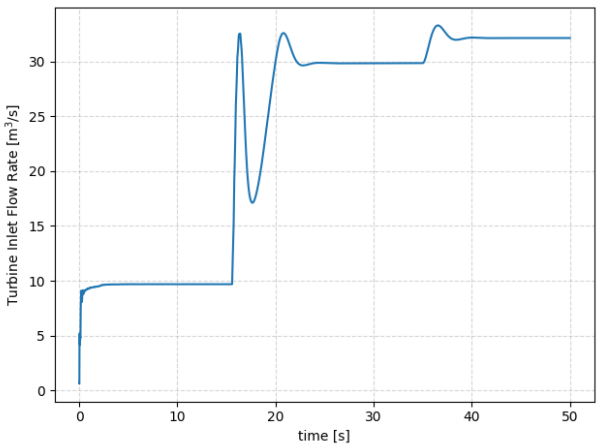

Figure 18. Flow rate through turbine vs. time.

Finally, the elastic flow model also produces results for the local wave speed and pressure-dependent density (Figure 19) and pipe diameter (Figure 20). The magnitude in the water density variation over the penstock is very small since the elastic modulus of the water is large. The local wave speed variations are also very small in magnitude, with the maximum local wave speed of 894.5 m/s and minimum wave speed of 894.2 m/s. The elastic pipe diameter variations are likewise small in magnitude, varying from 3.0 to 3.0008 m. This is due to the relatively large elastic modulus of the steel pipe and from the substantial thickness of the pipe walls. From these elastic deformation results, it is possible to also predict the hoop stress in the penstock pipe walls using the elastic flow model.

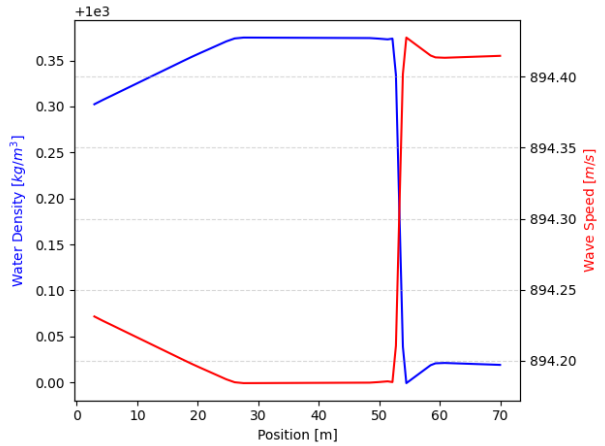

Figure 19. Density, ρ, and local wave speed, a, profiles at t = 50 s.

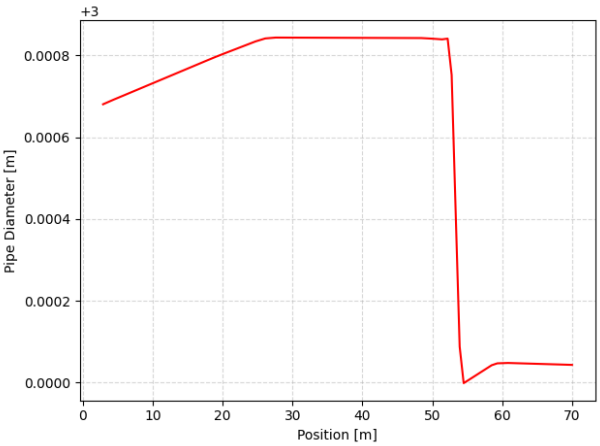

Figure 20. Pressure-dependent elastic pipe diameter at t = 50 s.

3.2 COMPARISON WITH INELASTIC MODEL RESULTS

The elastic flow model was compared against the inelastic model developed in previous work (Gurecky et al. [2022]) to understand the differences between the two modeling approaches. The same geometry, parameters, and turbine model were used in both the elastic and inelastic cases so that a direct comparison could be made for the mass flow rate, pressure, and turbine power and rotation rate results as a function of time. Additionally, the same turbine PID speed control method was used in both cases, and the same PID gain parameters were used in both models, as given in Table 1.

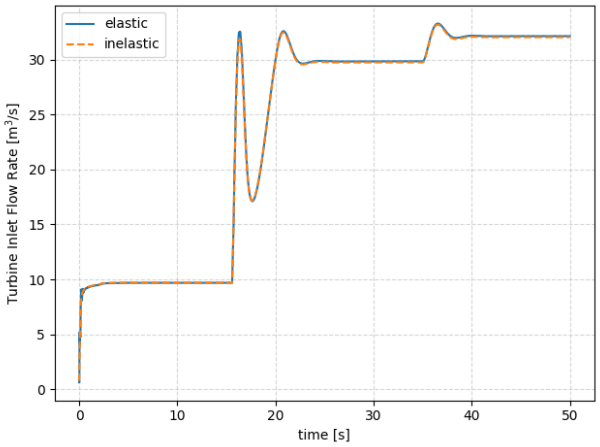

Figure 21. Elastic vs. inelastic model turbine flow rate.

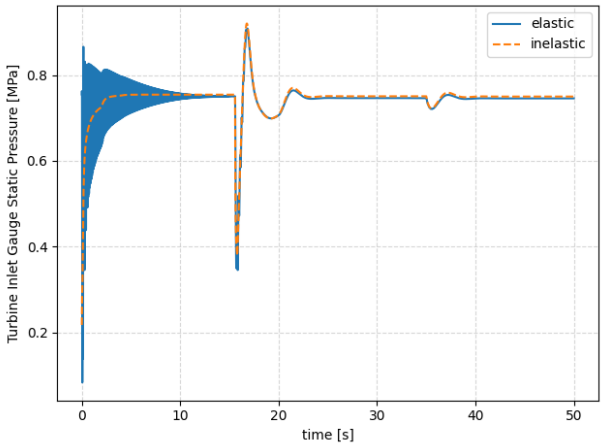

Figure 22. Elastic vs. inelastic model turbine inlet pressure.

At $t = 50$ s, the elastic flow model predicts a turbine flow rate of 32.137 m^3/s and the inelastic model predicts a steady-state flow rate of 32.038 m^3/s, an absolute difference of 0.099 m^3/s or a relative difference of 0.31%. This mass flow rate is ultimately determined by the pressure losses through the system, and available gravitational head; thus, if small differences are predicted in the pressure loss across the turbine section in the elastic vs. inelastic case, then the predicted mass flow rate will be slightly different. The overall agreement in this case is within 1% relative difference and is acceptable. Numerical experiment investigations showed that the elastic model–predicted pressure drop over the turbine was sensitive to the mesh spacing and can explain some portion of this difference in the steady-state value. The inelastic model has no mesh spacing option as it is an ordinary differential equation model that enforces the mass flow rate is always spatially uniform (only a function of time) in all sections of the system.

The turbine inlet pressure comparison in Figure 22 highlights that the elastic flow model shows significant differences in the pressure field, especially in the start-up sequence. This is more apparent when zooming into the transient sequences in Figures 26 and 30. The predicted peak pressures in the system, and thus peak hoop stresses on the penstock, can be significantly different when elastic water hammer effects are accounted for.

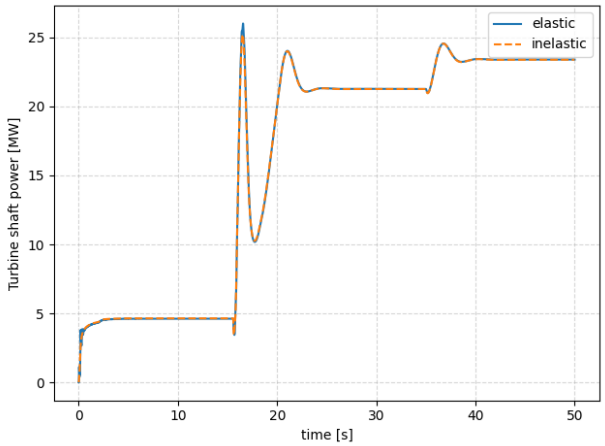

Figure 23. Elastic vs. inelastic model turbine power.

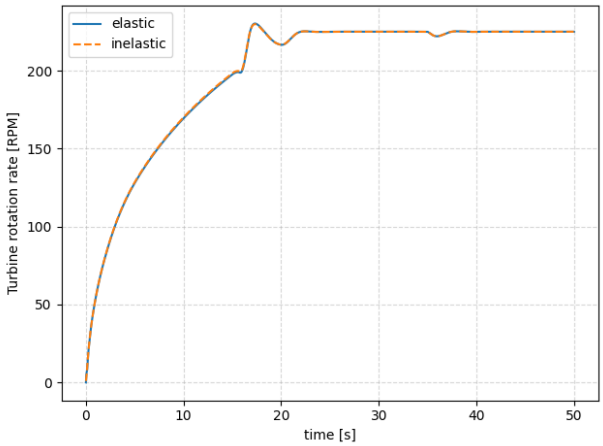

Figure 24. Elastic vs. inelastic model turbine rotation rate.

Good agreement is seen between the elastic and inelastic flow models for the turbine rotation rate and turbine shaft power in Figures 23, 24, and 28. Considering these quantities can be computed from basic energy conservation arguments, this agreement is expected.

When focusing on the transient time between $t = 0$ s and 8 s, the finer details of the elastic model–predicted pressure, flow rate, and turbine power become apparent. The rapid oscillations in these quantities is due to water hammer, where the elastic water column is slightly compressing and expanding in rapid succession, similar to a damped spring.

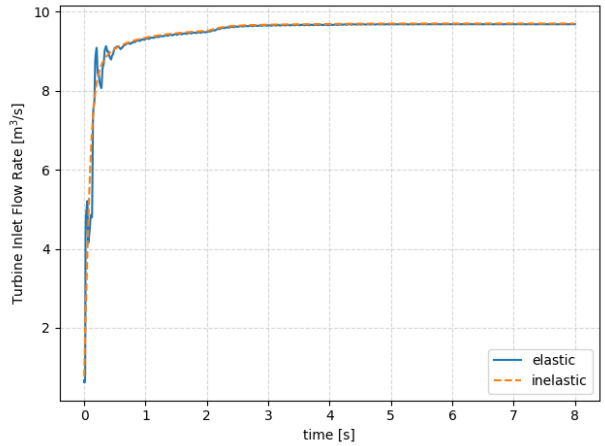

Figure 25. Elastic vs. inelastic model turbine flow rate.

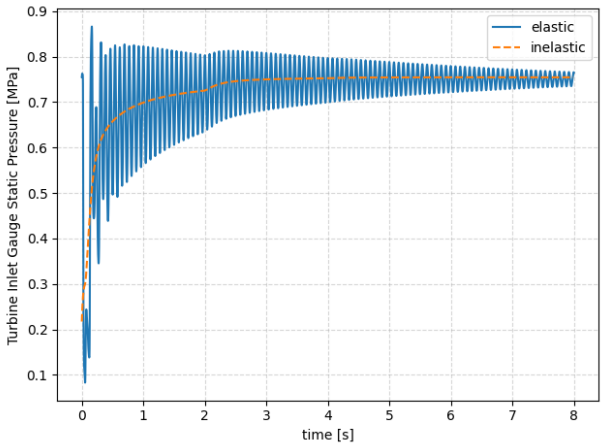

Figure 26. Elastic vs. inelastic model turbine inlet pressure.

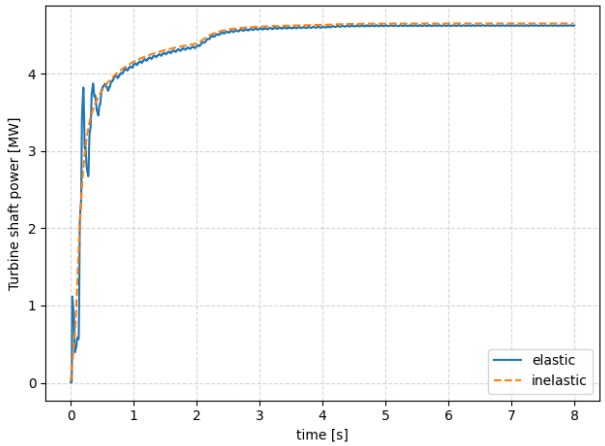

Figure 27. Elastic vs. inelastic model turbine power.

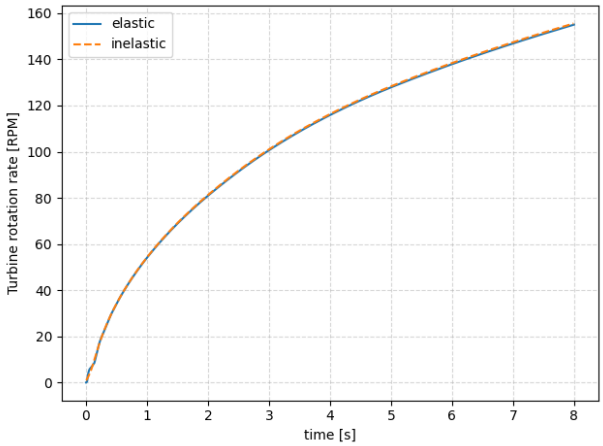

Figure 28. Elastic vs. inelastic model turbine rotation rate.

The transient time between t = 15 s and 25 s coincides with the rapid opening of the turbine inlet vanes and rapid applied torque increase. Figures 26 and 30 show that some pressure oscillations are captured by the elastic flow model that are not present in the inelastic model predictions; and in general, the pressure extrema predicted by the elastic flow model are greater in magnitude than the inelastic model. The minimum (e.g., vacuum condition in the draft tube shown in Figure 11) and maximum predicted pressures predicted by the elastic model are important quantities of interest for penstock design and analysis, particularly when estimating the maximum pressure loads experienced by the penstock under fast transient cases but also in estimating the long-term effects from water hammer and nonsteady loading patterns on the penstock and turbine. As shown in Figures 31 and 32, the agreement between the elastic and inelastic models for the turbine shaft speed and turbine power remains excellent.

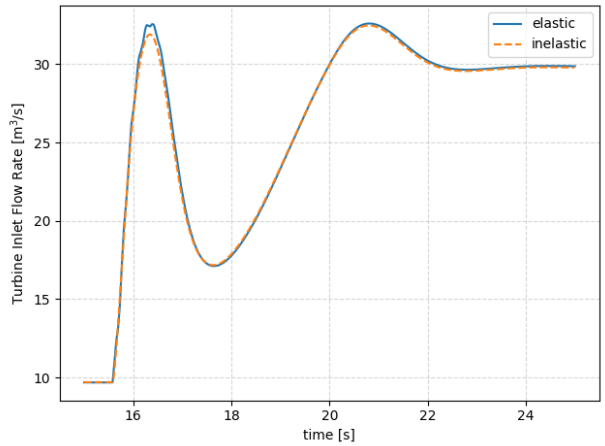

Figure 29. Elastic vs. inelastic model turbine flow rate.

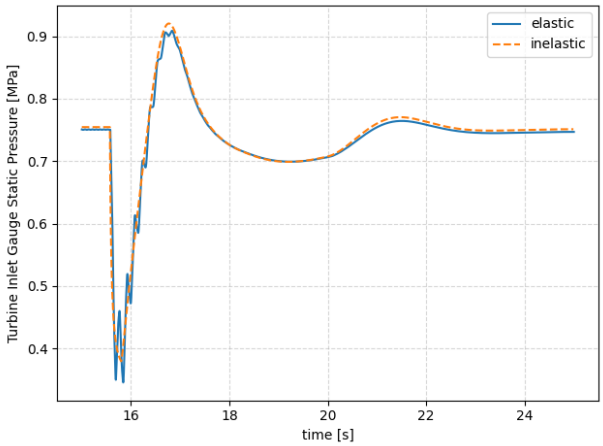

Figure 30. Elastic vs. inelastic model turbine inlet pressure.

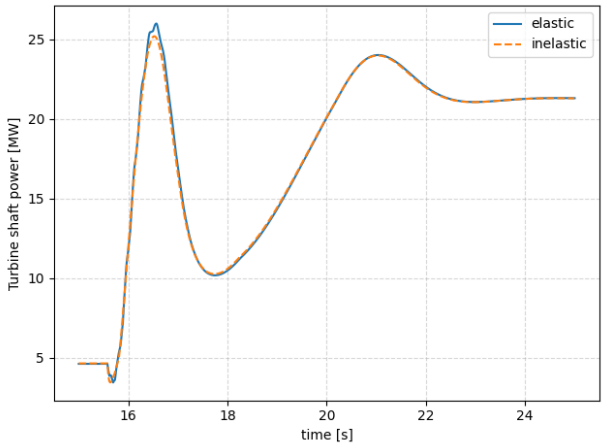

Figure 31. Elastic vs. inelastic model turbine power.

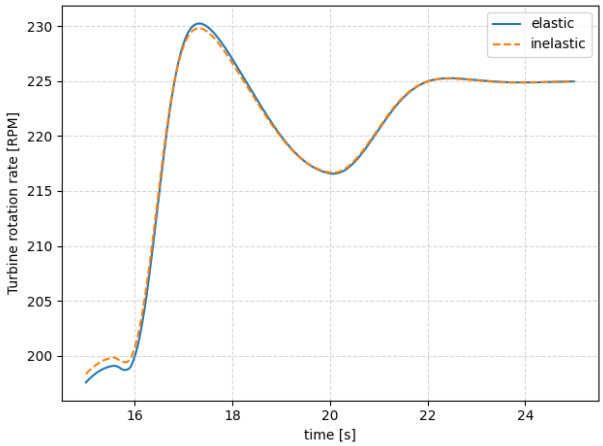

Figure 32. Elastic vs. inelastic model turbine rotation rate.

4. CONCLUSION

A finite volume–based elastic flow model was successfully implemented and applied to a hydropower system. The model included the entirety of the water system, including the penstock, turbine, and draft tube. The equations were solved using a cell-centered finite volume approach, where fluxes across cell boundaries were computed using the KT method, with cell interface values provided by the MUSCL scheme. This method proved successful in numerically solving the hyperbolic PDEs governing the elastic flow through the penstock system. This method is exceptionally flexible, offering the capability to handle nonconstant wave speed and to admit nonconstant mesh spacing. Results from this new elastic model were compared against results from a previously developed inelastic flow model.

The results demonstrate that the elastic flow model can capture fast dynamics, including the propagation of pressure transients encountered in water hammer computations. This capability might prove useful when estimating the system response to fast load changes, sudden blockages, or quick inlet vane movements. The results show that the elastic flow model offers additional details of the flow that are not resolved by the inelastic flow model, such as finely resolved space-and-time results for the water pressure, flow rate, water density, and local wave speed. In contrast, the mass flow rate and density in the inelastic flow model are uniform over the entire penstock because of the incompressibility assumption used in the inelastic model and because of mass conservation.

It is also shown that during slow transients—such as gradual valve opening and closing—and for estimating the steady-state flow rate of a hydropower system, the inelastic flow model produces a nearly identical result to the more computationally costly elastic flow model. From this result, we can conclude that the inelastic flow model is adequate for certain slow dynamic simulations and steady-state cases, which constitute the majority of hydropower plant operation. However, for fast transients or extremely long penstock systems, the elastic flow model provides more accurate estimates of pressure and flow rate inside the system, especially under fast load changes, sudden blockages, or fast guide vane movements.

In addition to the results generated by applying the model to an example hydropower system, the model was applied to a simplified linear advection problem in order to compare the numerical results against a known analytic solution, and to quantify the convergence rate of the implemented methods as a function of mesh spacing. The mesh convergence results are provided in Appendix A. From these results, we conclude that for the linear advection problem, the implemented KT and MUSCL scheme achieves second order, or an $O(\Delta s^2)$ convergence rate under smooth solutions to the PDE. For non-smooth solutions with jumps, the method was shown to converge with $O(\Delta s^{0.79})$. A more comprehensive verification of the implemented numerical methods offers avenues for future work.

Both the elastic and inelastic flow models were implemented in the Python programming language and offer a flexible interface that can be used to quickly build models of the water system for any given hydroelectric facility. Though a simplified dam penstock geometry was used as a demonstration in this report, the elastic flow model is applicable to many other hydropower facilities. The elastic flow model was implemented as a generic hyperbolic PDE solver, upon which a simple front-end application programming interface (API) was developed for hydropower system simulation. This API allows a user to add pipes, turbines, and pipe components to build up an arbitrary pipe network. In this way, any pipe system with a variety of sink and source terms stemming from turbines, pumps, pipe bends, valves, and other minor loss sources can be simulated. Note that the code is similar in capability to OpenHPL (Vytvytskyi and Lie [2019]), a hydropower model library for OpenModelica (Vytvytskyi [2019]); however, the models developed in the present work require familiarity with Python only and can easily interface with

Python-based machine learning libraries. In future work, we will target replacing portions of the turbine model, and potentially friction loss coefficients, with data-driven machine learning models such as neural networks. Data gathered from CFD and plant-measured sources will be used to train the models. The elastic and inelastic code was developed with these future machine learning tasks in mind.

5. ACKNOWLEDGMENTS

This work was supported by the DOE Water Power Technologies Office and used resources at the National Transportation Research Center at Oak Ridge National Laboratory, a User Facility of DOE's Office Energy Efficiency and Renewable Energy.

6. REFERENCES

M. Arora and P. L. Roe. A well-behaved tvd limiter for high-resolution calculations of unsteady flow. *Journal of Computational Physics*, 132(1):3–11, 1997.

M. H. Chaudhry. *Applied hydraulic transients*, volume 415. Springer, 2014.

J. Gale and I. Tiselj. Water hammer in elastic pipes. *International Conference Nuclear Energy in Central Europe*, 2002. URL https://www.osti.gov/etdeweb/biblio/20542833.

J. L. Gordon. Hydroturbine cavitation erosion. *Journal of Energy Engineering-asce*, 118:194–208, 1992.

W. Gurecky, H. Wang, and S. Ou. One dimensional penstock flow models for hydropower digital twin. Technical report, Oak Ridge National Lab.(ORNL), Oak Ridge, TN (United States), 2022.

A. Kurganov and E. Tadmor. New high-resolution central schemes for nonlinear conservation laws and convection–diffusion equations. *Journal of computational physics*, 160(1):241–282, 2000.

B. Muson, D. Yound, H. Okiishi, and W. Huebsch. *Fundamentals of Fluid Mechanics*. 2009.

P. Roe. Approximate riemann solvers, parameter vectors, and difference schemes. *Journal of Computational Physics*, 43(2):357–372, 1981. ISSN 0021-9991. doi: https://doi.org/10.1016/0021-9991(81)90128-5. URL https://www.sciencedirect.com/science/article/pii/0021999181901285.

M. Szydłowski. Finite volume method for water hammer simulation. *TIASWiK, Poland*, 2002.

G. D. Van Albada, B. Van Leer, and W. Roberts Jr. A comparative study of computational methods in cosmic gas dynamics. *Astronomy and Astrophysics, vol. 108, no. 1, Apr. 1982, p. 76-84.*, 108:76–84, 1982.

B. Van Leer. Towards the ultimate conservative difference scheme. ii. monotonicity and conservation combined in a second-order scheme. *Journal of computational physics*, 14(4):361–370, 1974.

L. Vytvytskyi. User's guide for the open hydropower library (openhpl). *University of South-Eastern Norway, Porsgrunn, Norway*, 2019. URL https://build.openmodelica.org/Documentation/OpenHPL%201.1.1/Resources/Documents/UsersGuide.pdf.

L. Vytvytskyi and B. Lie. Mechanistic model for francis turbines in openmodelica. *International Federation of Automatic Control Conference Proceedings*, 51, 2018.

L. Vytvytskyi and B. Lie. Openhpl for modeling the trollheim hydropower plant. *Energies*, 12(12):2303, 2019.

E. B. Wylie and V. L. Streeter. Fluid transients. *New York*, 1978.

APPENDIX A. Mesh Convergence Study

A mesh convergence study was performed on a simplified one-dimensional linear advection problem of the form:

$$\frac{\partial C}{\partial t} + v_s \frac{\partial C}{\partial s} = 0$$

with the velocity held constant, $v_s = 1$ m/s . C represents an arbitrary species concentration.

Two cases were examined. The initial concentration profile in the first case was a smooth normal distribution: $C(s, t = 0) = N(\mu = 2, \sigma = 0.5)$. In the second case the initial concentration profile was a square wave of width 2 m, centered at 2 m and wave magnitude of 1. In both cases, the domain is bounded by $s = 0$, and $s = 10$ m.

The results shown in figures 33 and 34, are visualized at t =3 s, after the wave was advected such that the wave is centered at s=5 m. For these two cases the analytic solution is trivial and the exact result can be used to investigate the numerical method's performance under smooth solutions and solutions which contain discontinuities. Since no diffusion term is present in this case, a higher performing solution method will preserve the initial shape of the concentration wave, with minimal artificial dissipation as it is advected from the left to the right of the domain.

The mesh convergence results for the smooth wave advection case are tabulated in Table 2 and visualized in figure 35. For the square wave problem, the results are shown in table Table 3 and figure 36. The KT and MUSCL based method exhibits second order ($O(\Delta s^{2.04})$) spatial convergence of the mean absolute error (MAE) for the smooth wave advection case. For the square wave case with discontinuities, the MAE converged sub-linearly at $O(\Delta s^{0.79})$. For smooth solutions, the KT scheme with a piecewise-linear MUSCL reconstruction is expected to give a quadratic convergence rate. A similar linear advection mesh convergence study is detailed by Kurganov and Tadmor [2000] with the L_1 error shown as having quadratic convergence in cases without shocks. In cases where discontinuities are present in the solution, Kurganov et. al. use a different norm, the Lip$'$ norm, since the convergence rate near the discontinuity is locally different than in smooth regions of the solution. In the square wave case, the flux limiter is required to maintain the stability of the solution; however, the reliance on the limiter results in a degradation of the convergence rate in cells immediately adjacent to the discontinuities. In this case, the superbee limiter was used.

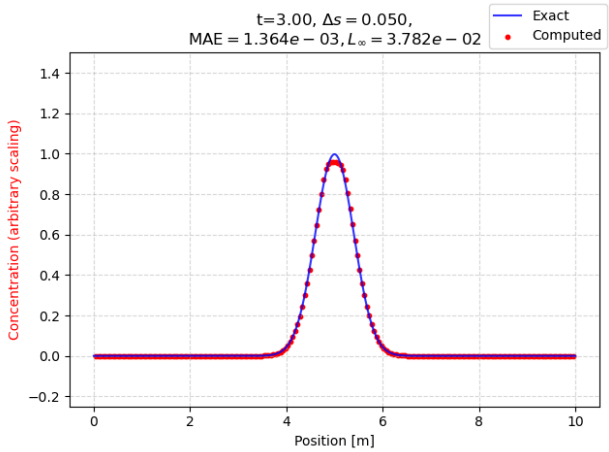

Figure 33. Smooth wave advection solution at $t = 3(s)$ with mesh spacing $\Delta s = 0.05(m)$.

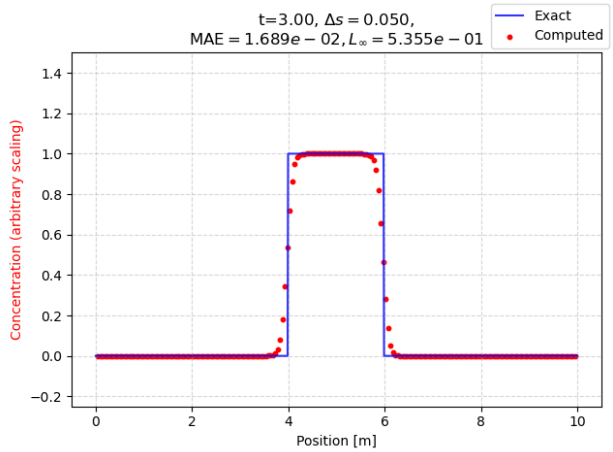

Figure 34. Square wave advection solution at $t = 3(s)$ with mesh spacing $\Delta s = 0.05(m)$.

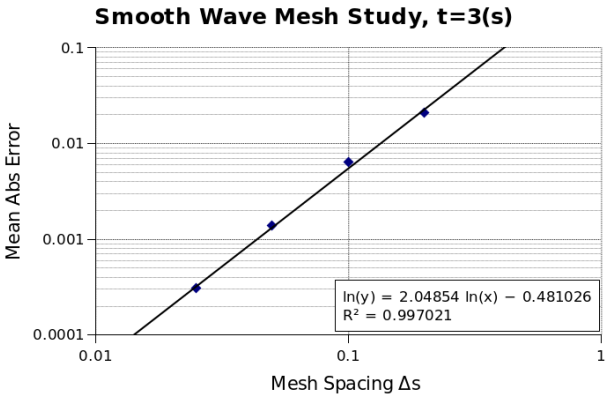

Figure 35. Mesh spacing convergence plot for the smooth wave advection problem

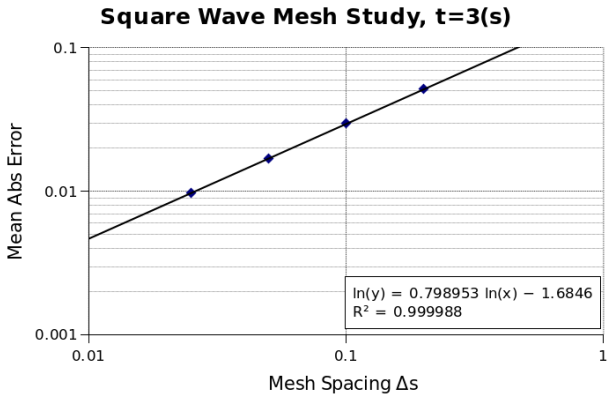

Figure 36. Mesh spacing convergence plot for the square wave advection problem.

Table 2. Smooth wave mesh convergence results.

N	Δs	MAE	L_∞
50	0.2	0.02080	0.2176
100	0.1	0.006307	0.09821
200	0.05	0.001364	0.03782
400	0.025	0.0003049	0.01357

Table 3. Square wave mesh convergence results.

N	Δs	MAE	L_∞
50	0.2	0.05137	0.5499
100	0.1	0.02944	0.5417
200	0.05	0.01689	0.5355
400	0.025	0.00976	0.5307